Nuclear accessibility of β-actin mRNA is measured by 3D single-molecule real-time tracking

Carlas S. Smith,[1]* Stephan Preibisch,[2,3,4]* Aviva Joseph,[1] Sara Abrahamsson,[3,5] Bernd Rieger,[6] Eugene Myers,[3,4] Robert H. Singer,[2,3] and David Grunwald[1]

[1]RNA Therapeutics Institute, University of Massachusetts Medical School, Worcester, MA 01605
[2]Department of Anatomy and Structural Biology, Albert Einstein College of Medicine, Bronx, NY 10461
[3]Howard Hughes Medical Institute Janelia Farm, Ashburn, VA 20147
[4]Max Planck Institute of Molecular Cell Biology and Genetics, Dresden 01307, Germany
[5]The Rockefeller University, New York, NY 10065
[6]Department of Imaging Sciences, Technical University Delft, Delft 2628CJ, Netherlands

Imaging single proteins or RNAs allows direct visualization of the inner workings of the cell. Typically, three-dimensional (3D) images are acquired by sequentially capturing a series of 2D sections. The time required to step through the sample often impedes imaging of large numbers of rapidly moving molecules. Here we applied multifocus microscopy (MFM) to instantaneously capture 3D single-molecule real-time images in live cells, visualizing cell nuclei at 10 volumes per second. We developed image analysis techniques to analyze messenger RNA (mRNA) diffusion in the entire volume of the nucleus. Combining MFM with precise registration between fluorescently labeled mRNA, nuclear pore complexes, and chromatin, we obtained globally optimal image alignment within 80-nm precision using transformation models. We show that β-actin mRNAs freely access the entire nucleus and fewer than 60% of mRNAs are more than 0.5 µm away from a nuclear pore, and we do so for the first time accounting for spatial inhomogeneity of nuclear organization.

Introduction

The nucleus of a cell is a crowded, compartmentalized volume wherein dynamic and complex biochemical and molecular events occur. For example, mRNAs are transcribed, spliced, released from the transcription site, and subsequently move to the nuclear periphery where they are exported to the cytoplasm to be translated into proteins.

The nuclear landscape in which these processes take place is spatially complex. The genome is organized into topological domains, which in turn organize into nonrandom chromosome territories (Gibcus and Dekker, 2013). Adding to this complexity are functional distinct compartments or nuclear bodies, such as the nucleolus, histone locus bodies, splicing speckles, and others (Padeken and Heun, 2014). The nuclear landscape is also temporally complex (Misteli et al., 2000; Phair and Misteli, 2000); nuclear bodies show high turnover rates of their components (Sleeman and Trinkle-Mulcahy, 2014) and the nucleus as a whole undergoes major reformation during the cell cycle (Schermelleh et al., 2008; Cook and Marenduzzo, 2009; Shevtsov and Dundr, 2011; Sleeman and Trinkle-Mulcahy, 2014). Directly studying the dynamics of nuclear components, such as mRNAs in the nucleus of a living cell, will help to define the rules that govern the kinetics, locations, and interactions of proteins and nucleic acids relative to nuclear structure.

Advanced microscopy techniques have improved image resolution or enabled fast tracking of individual molecules in living cells, allowing the nuclear mobility of different proteins, RNAs, and other molecules to be probed (Görisch et al., 2004; Shav-Tal et al., 2004; Politz et al., 2006; Grünwald et al., 2008). Currently available single-molecule imaging methods share the limitation that they can only image fast enough to accurately track single molecules in one optical plane (2D) or their 3D capability only allows visualization of small numbers of molecules within a limited field of view (Ragan et al., 2006; Huang et al., 2008; Backlund et al., 2012). Conventional 3D imaging

*C.S. Smith and S. Preibisch contributed equally to this paper.

Correspondence to David Grunwald: david.grunwald@umassmed.edu

Abbreviations used in this paper: 3D-SMRT, 3D single-molecule real-time tracking; CCG, chromatic correction grating; EMCCD, electron multiplying charge coupled device; eYFP, enhanced YFP; MFG, multifocus grating; MFM, multifocus microscopy; NPC, nuclear pore complex; PSF, point spread function.

The Rockefeller University Press $30.00
J. Cell Biol. Vol. 209 No. 4 609–619
www.jcb.org/cgi/doi/10.1083/jcb.201411032

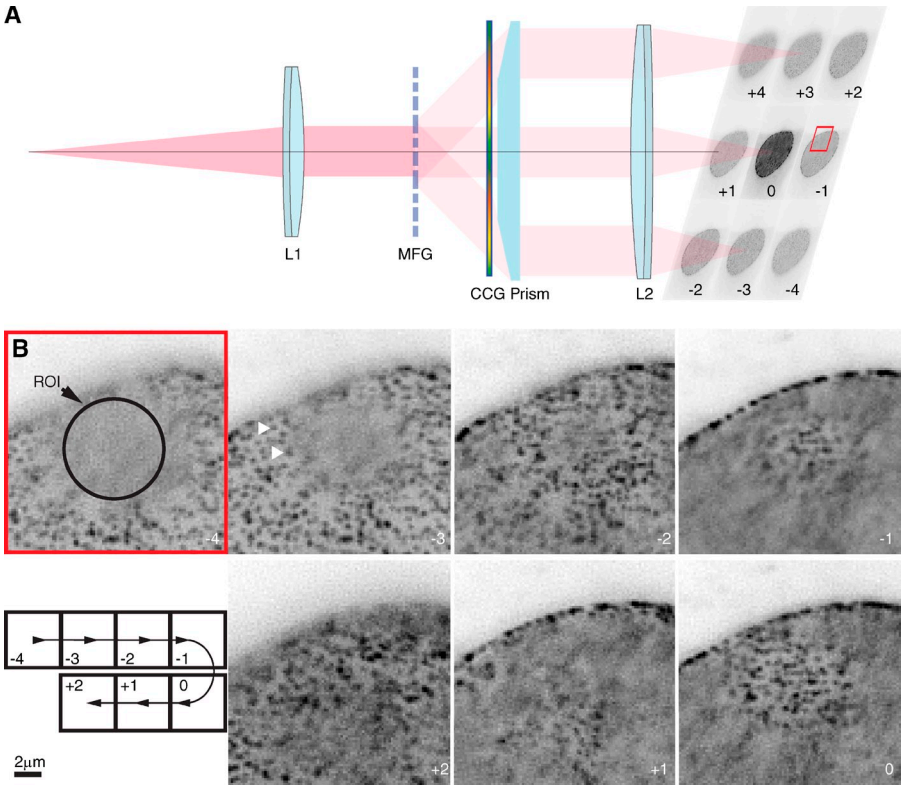

Figure 1. **Simultaneously acquired 3D image of the nuclear envelope.** (A) Schematic drawing of the multifocus relay optic enabling simultaneous 3D image acquisition. The lens L1 forms a secondary Fourier plane (an image of the objective pupil) in which the MFG is placed to split the beam into zero- and first-order diffraction beams. Lens L2 forms the secondary image plane on the camera. The first-order diffraction forms eight beams around the zero order with only the above (+3) and below (−3) beams depicted. The zero-order beam travels straight through an empty panel in the CCG, the central, flat facet of the prism, and is focused on the camera by L2. The first-order beams are separated and refocused by the MFG, corrected for chromatic dispersion by the CCG, redirected to proper positions on the camera by the prism, and focused onto the camera by L2. An example of the nine image planes (NPC image recorded in the red channel) projected in a 3 × 3 array and simultaneously recorded by a CCD camera is shown. Numbers on the subfields of the image correspond to the relative position of the plane in the stack. (B) A magnified series of a region of interest from A (red box) shown over seven planes (planes +3 and +4 not shown as out of focus). Arrowheads (plane −3) point to nuclear pores and the circle marks unexpected invagination. The region of the nuclear envelope that is out of focus near the bottom of the cell comes into focus near the middle of the cell. Image is shown with black and white values inverted.

with wide-field light microscopes requires a series of images to be taken along the optical (z) axis. The time required to move the objective and sample relative to each other introduces a time delay that can be significant enough to prevent 3D tracking of fast-moving molecules. Furthermore, measuring the kinetics of single molecules relative to nuclear structure requires the accurate registration of image information from two or more different channels (Grünwald and Singer, 2010). Perhaps more challenging is the need to image at physiologically tolerable excitation powers and the ability to detect weak signals (Carlton et al., 2010). Thus, sensitive microscopy methods that can quickly acquire high-resolution images and track single molecules in 3D volumes are needed (Trinkle-Mulcahy and Lamond, 2007).

Extracting information from a 3D volume into a single image plane, for example, using astigmatism, double helix spiral phase microscopy, or techniques that simultaneously image multiple focal planes in biplane or multifocus microscopy (MFM; Huang et al., 2008; Ram et al., 2008; Backlund et al., 2012; Abrahamsson et al., 2013), is one way to circumvent sequential z-stack imaging and instead simultaneously image 3D volumes. We recently developed MFM as a method to track single molecules in 3D volumes. Here we combine the technique with precise image registration between fluorescently labeled mRNA, nuclear pore complexes (NPCs), and chromatin for 3D single-molecule real-time tracking (3D-SMRT). We present an image processing solution to convert the recorded images into well-aligned z-stacks. This solution consists of image registration between each plane, calculation of the correct z-position of each plane in each color channel, and registration between color channels. The same multifocus optics are used for all color channels, causing a color-dependent difference in z-spacing between the focal planes as well as a slight magnification difference. We developed a transformation model to compensate for sample-induced aberrations and chromatic differences to enable global alignment of images within half-pixel precision. Finally z-stack images are deconvolved and further analyzed. As a result we can resolve the relationship between DNA-dense regions, the nuclear periphery, and the spaces occupied by mRNA moving through the nucleus. We show statistically that β-actin mRNAs freely access the entire nuclear space and that most (60%) are within 0.5 µm of nuclear pores.

Results

Reconstructing multicolor movies of single molecules in 3D

We have applied MFM to image weak fluorescent signals of labeled mRNAs in the nucleus of a live cell and developed an image-processing framework (Preibisch et al., 2010) that relies on inherent registration markers (Grünwald and Singer, 2010). To understand if nuclear structure, particular chromatin organization, impacts β-actin mRNA movement between its site of transcription and nuclear pores, we built a microscope to simultaneously image multiple focal planes with two different fluorescent channels. After the tube lens of the microscope, we attached the multifocus optics that split the detection light into nine planes along the optical axis of the objective (Abrahamsson et al., 2013; Fig. 1 A). Mouse fibroblast cells were imaged in which all β-actin mRNAs are labeled with enhanced YFP (eYFP) fused to the MS2 coat protein, nuclear pores are fluorescently labeled with tdTomato fused to POM121, and heterochromatin are stained with a violet vital dye (Vybrant

DyeCycle Violet) that emits fluorescent signal over the entire spectral range. Zooming in on the nuclear pore stain (Fig. 1 B) illustrates the power of simultaneous 3D imaging, even before quantitative image analysis. The section of the nucleus shown has an invagination of the nuclear envelope resulting in patches of nuclear pores being in focus (Fig. 1 B, arrowheads) and out of focus (Fig. 1 B, circle).

We acquired time series of both the nuclear pore and β-actin mRNA simultaneously on two cameras with a frame rate of 10 Hz for up to 30 s using a 514- and 561-nm laser for excitation. The power at the back-focal plane was measured to be ∼600 µW. Using eYFP to label mRNA via MS2 coat protein, photobleaching was the limiting factor for acquisition duration. Within 1 s after acquiring the nuclear pore and mRNA data, we image the DNA stain on both cameras for 1 s followed by the acquisition of a Piezo-driven z-stack with 10-nm steps. DNA images were used as a reference for image processing, to align images in each channel and to register the β-actin mRNA and nuclear pore channels.

Lateral image registration

During imaging, the emission signal is split into nine planes using a diffraction grating and the nine planes are recorded in an array on the camera. Because of imperfections in the MFM optical train, the nine subimages (Fig. 1 A) are slightly rotated relative to each other (Fig. 2 A) and need to be aligned laterally. The two fluorescent channels are recorded on separate cameras resulting in spatial offsets between them that need to be corrected for. The reference point in this alignment is the inherent DNA stain that can be excited specifically at 405 nm and emits over the whole visible range such that we can record identical images in both fluorescence color channels. The DNA stain fluorescence is used to align each channel over the nine planes and both color channels relative to each other. The lateral image data provides sufficient resolution (∼250 × 250 pixels/plane) to compute 2D rigid transformation models and apply them to each imaging plane in each channel using image interpolation (Fig. 2 B).

To achieve a globally optimal lateral image alignment, we first performed geometric local descriptor matching (Preibisch et al., 2010). Gaussian-shaped signals in the nine registration images of the DNA stack were extracted for each image plane using the Difference-of-Gaussian detector combined with a 2D-quadratic fit for subpixel localization (Brown and Lowe, 2002). The goal is to identify corresponding points and to use those corresponding points to determine the transformation for all planes. To achieve this, each candidate point is expressed as a geometric local descriptor consisting of the candidate point itself and its n nearest neighboring points (Fig. 2 C), where translation-invariant geometric local descriptor matching is used to compute the similarity between two descriptors (Preibisch et al., 2010). As Difference-of-Gaussian detections inside the sample are likely to contain random, noncorresponding detections, we add redundancy to the matching process (Fig. 2 D). For each candidate point $n + 1$ nearest neighbor points are extracted and all combinations of n neighboring points are matched, where the best combination of any subset of both descriptors defines

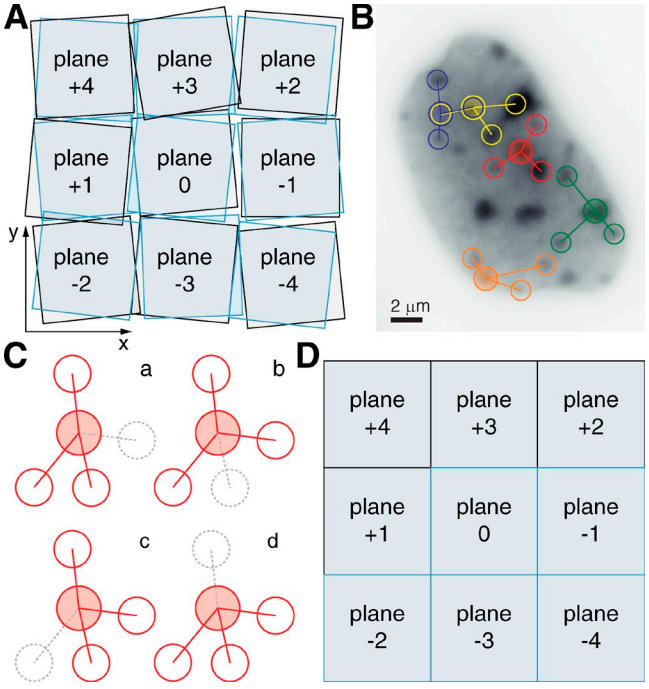

Figure 2. **Lateral image registration.** (A) Two-channel alignment of lateral image data as acquired by the camera. Black and blue panels represent the two-color channels. Numbers indicate the relative position of each panel in the stack. (B) Image of the DNA stain used for image alignment overlaid the detection of blob-shaped interest points used as redundant geometric local descriptors to compute the lateral rigid transformations in A. (C) Illustration of the redundancy used for matching of geometric local descriptors. (D) Illustration of camera image after successful lateral alignment.

their similarity. Corresponding candidate pairs between two descriptors are assigned if the best match for a descriptor shows significantly better similarity (3×) than the second best matching descriptor. Comparing all descriptors of one image plane against all descriptors of another image plane yields a collection of corresponding candidates. Spurious matches are filtered using RANSAC (Fischler and Bolles, 1981) on a rigid transformation model, yielding a list of true corresponding descriptors. Exhaustively matching the set of all image planes provides all corresponding descriptors, linking together all image planes over all channels. Globally minimizing the distance between all corresponding points (Saalfeld et al., 2010) results in an optimal rigid transformation model for each plane (Fig. 2 D and Video 1). This allows us to create a 3D stack for each image recorded and assess how well it is aligned.

Axial image registration

The spectral red-shift between eYFP and tdTomato causes deviations in z-step size between both color channels (Fig. 3 A). Sample-induced aberrations along the z axis cause an additional defocus in the image stack above and below the center plane. This effective defocus must be estimated quantitatively before further image restoration can be performed by image deconvolution. Therefore, additional axial image registration is required. Axial image alignment was performed independent of the lateral registration because of the significant sampling difference, 160 nm lateral with ∼250 pixels per plane and 250 nm axial

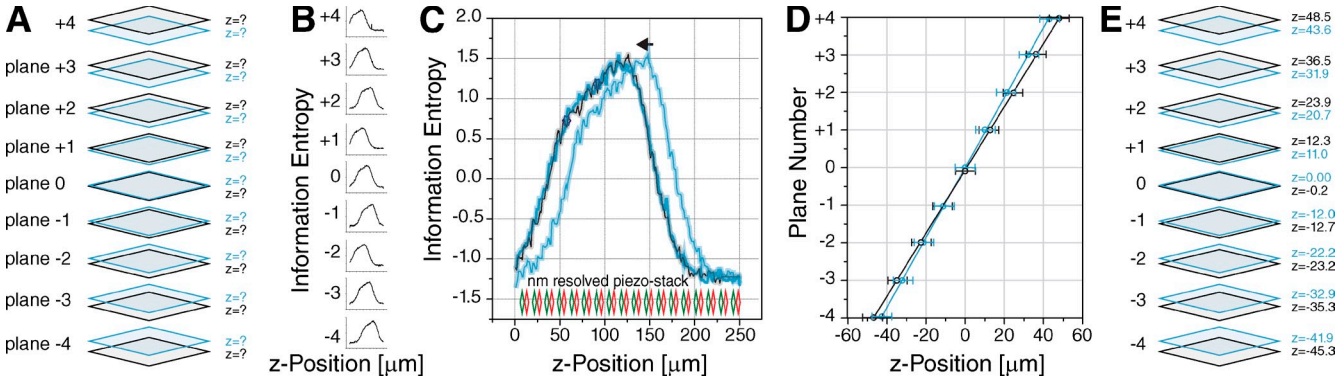

Figure 3. **Axial image registration.** (A) Final lateral (x and y) and missing axial (z) position of each plane in the two fluorescent channels (gray and black frames). (B) To determine the correct axial (z) position for each imaging plane the information entropy is computed over the entire axial range of the imaged cell using a stack acquired for each cell using a Piezo stage with nanometer step size. Maxima in the entropy function of each plane mark the point where the center of the image is in focus in each plane. (C) As the DNA signal is recorded in both channels, pairwise matching of the nine entropy functions from both channel stacks yields a set of 153 relative distances. For robustness of the method, outliers are removed. The axial offset is the distance the gray entropy curve needs to be shifted (arrow) to optimally overlap with the black entropy curve. Black and gray represent the two fluorescent channels. (D) Data in each channel were fit to individual linear functions yielding the final relative position of each image plane in its stack. Because of the resolution of nine z-planes, transformations are not applied to avoid image artifacts but instead applied to all extracted coordinates during subsequent analysis steps. (E) Fully aligned stack of all nine planes recorded by the camera. Each cell is sampled with 10-nm step size once, resulting in $n = 153$ distance measures for registration. The error is dominated by the step width of the Piezo to ±5 nm indicated either as line width in C or as error bar in D.

with only nine planes, as well as the different type of transformation models used in each dimension, lateral (x and y) and axial (z).

The axial position of all individual planes is described by 1D translation models, whereby the axial position of each image plane is computed by combining pairwise matching of autofocus-like functions with model-based outlier removal (Fischler and Bolles, 1981) and global optimization (Saalfeld et al., 2010). To do so we make use of the finely resolved second registration dataset that is acquired using the stepping of the MFM volume along the optical axis of the microscope using a Piezo stage. First, the entropy function for the Piezo stacks of all image planes and channels is computed (Fig. 3 B) and the information content for each individual z-slice of every Piezo stack is measured, with the information content being highest in the center of the sample. As the finely resolved stack of 3D-SMRT volumes covers the entire sample for every image plane, the shape of each function is similar (Fig. 3 B) but shifted in axial position (Fig. 3 C). All entropy functions are pairwise registered with each other using a simple gradient descent (Fig. 3 C) yielding all pairwise axial distances between all image planes. For each channel, all axial positions can be fitted using a linear function (Fig. 3 D). This allows us to remove outliers in the pairwise entropy alignment (Fig. 3 C) using RANSAC on a linear function fit. Global minimization of all pairwise axial distances between all remaining inliers from all channels yields the final positions of all image planes of all channels (Fig. 3 D). The slope of the linear fit along the z axis is a function of the emission wavelength, as expected by the design of the multifocus grating (MFG; Abrahamsson et al., 2013). The registration image data directly yields the chromatic shift along the z axis. The correction is not applied to the image data to avoid interpolation artifacts that would result from the correction value not exactly matching the 250-nm axial sampling between the nine planes. Instead, the axial position of each plane is directly applied to all coordinates during subsequent analysis steps (Fig. 3 E and Video 1). After deconvolution, it is now possible to quantify distinct features in the image volume.

Image registration precision

We found it both important and necessary to have a measure for success or failure of the image alignment, as many parameters impact the image registration performance. Such parameters include the number of descriptor pairs; cutoff values for outlier removal; the transformation model used (translation vs. rigid vs. affine vs. homography) or the homogeneity of feature distribution over the sample; stain and shape of features; and the general geometry of the application. In general, the fewer the corresponding features (signals used to register the images) to be aligned the more precise the registration of these features will be. To achieve uniform alignment over the whole object of interest, in our case the nucleus, the more sampling points, the more homogenous their distribution, and the lower the remaining error, the better the global alignment will be.

We used a rigid transformation model and a global alignment target of 0.5-pixel cutoff value for outlier removal (RANSAC). The image registration precision therefore was determined as the higher bound of an image alignment deemed acceptable. To assess if the registration value targeted was achieved or realistic for the dataset, the remaining distance of all corresponding features was measured and plotted as a histogram (Fig. 4, A and B). We found that both x and y components were distributed normally and are well described by a Gaussian curve. The "width" of these resulting distributions is a measure of precision, σ, for the achieved registration. We found that the remaining error after alignment of the cell nucleus data using the inherent DNA marker for 7,387 corresponding features had a width of 0.44 pixels for the x ordinate (Fig. 4 A) and 0.39 pixels for the y ordinate (Fig. 4 B), well below our target

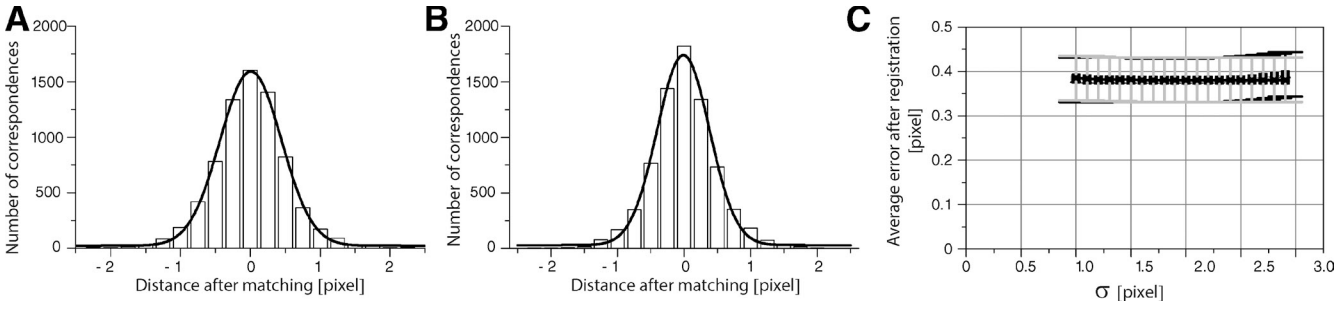

Figure 4. **Global registration precision.** (A and B) Distribution of remaining distances between $n = 7{,}387$ registration features after registration with a rigid 2D transformation model for a single cell. No bias (mean value is zero and distribution symmetric) was introduced and the width σ for x (A) is 0.44 pixels or 70 nm and for y (B) is 0.39 pixels or 62 nm. A and B represent the error of the lateral alignment in x and y as laid out in Fig. 2 for a single cell with a target of σ = 0.5-pixel global registration precision. (C) Two kinds of beads were embedded in an agarose gel. First the diffraction-limited beads were aligned using a Gaussian fit for the center of the bead location, which was then used for alignment. Alternatively, the beads (1-µm diameter) were aligned using a quadratic fit for corresponding features. The remaining mean error after registration relative to the σ used for fitting is shown. The differences between both methods are within the noise level at <1 nm. The total error of the alignment is dominated by the localization precision (here 10 nm; error bar in C).

of 0.5 pixels. An even higher precision can be achieved after focus shift correction, but only for the registration signal. This is because the registration signal is not a single MFM volume, but a nanometer-resolved z-scan of many MFM volumes over the z-range of the MFM volume used for tracking. We used these alignment Piezo stacks to calculate the z-offset that we correct for after localization in the x,y plane (Figs. 2 and 3). If one overlays these two perfectly z-matched image planes, the x,y registration is higher than for the experimental data. The next point of interest is if the alignment has a bias, or what is the accuracy of the alignment? As can be seen in Fig. 4, the mean of the distribution is zero and symmetric (measure of accuracy), which agrees with the nature of stochastic errors, whereas the width σ is <0.5 pixels (measure of precision).

Next we used an artificial sample of known structure to test image alignment under defined conditions. Beads of 1-µm diameter were labeled with plasmid DNA, which was stained with Vybrant DyeCycle Violet and embedded together with 200 nm of TetraSpeck beads in 1% agarose. The green and red image stacks were aligned in one of two ways: using feature-based alignment of the larger beads with a 0.5-pixel precision target or based on the point signals from the TetraSpeck beads. The agarose introduced minor aberrations compared to cells, providing a best-case test scenario. As expected, the resulting alignment was better than for the cell data in both cases (Fig. 4 C). Gaussian fitting of the fluorescent beads with widths close to that of the point spread function (PSF) in a low-scattering, homogenous medium or sample, such as the gel used in our control experiment (Fig. 4), was not superior to the feature-based alignment providing a subnanometer smaller final registration error. A subnanometer difference is within the noise limit of the method and therefore insignificant. The feature-based alignment (Fig. 4 C) proved more robust for irregular or blurred signals/image features. In practice, the Gaussian fitting of point-like bead signals neglects aberrations introduced by the sample itself, whereas feature-based registration (Fig. 4, A and B) allows sample-induced aberrations described by the transformation model to be corrected for and is also more robust (Fig. 4 C).

3D-SMRT imaging of live cells

Our aim was to test if specific areas exist in the nucleus of living cells that are correlated with how mRNAs reach the nuclear periphery and if heterochromatin contains a lower level of mRNAs than found, on average, within the nucleoplasm. To validate our nuclear pore tag as a marker for the nuclear envelope we counted the number of NPCs per micrometer squared at the focal planes closest to the objective (Fig. 1 B). We found that there are approximately one to four NPCs per micrometer squared, as previously reported using confocal microscopy (Kubitscheck et al., 1999). 3D-SMRT microscopy directly visualizes β-actin mRNA movement with relation to dense and sparse DNA volumes within the nucleus (Fig. 5 A), which correlates to heterochromatin-rich and -poor regions. The ability to detect the relative positions of DNA, mRNA, and NPCs from different angles, instead of in 2D planes that often contain out-of-focus signal, allows rigorous interrogation of possible colocalization events (Fig. 5, B and C). The ability to record volumetric movies makes it possible to track molecules and nuclear structure over time (Fig. 5, D–G). After image deconvolution, the image volumes still contain noise, but the signal is defined by its localized intensity caused by the multiple binding sites on the mRNA (Fig. 5 H). To understand nuclear occupation by β-actin mRNA intensity, thresholds were manually selected to best fit the dense DNA volume, which we refer to as heterochromatin. An additional lower intensity threshold was selected that corresponded with volumes surrounding the high intensity DNA signal, which we refer to as periphery. Any remaining space within the nuclear envelope, defined by the nuclear pore stain, is referred to as nucleoplasm. Thresholds were confirmed to be comparable between cells using an analysis of variance test. Visual comparison of staining patterns of Vybrant DyeCycle Violet live-cell DNA stain to fixed-cell DNA stains (e.g., Hoechst or DAPI) indicates that they correspond well with each other. This result is in agreement with a previous study (Schermelleh et al., 2008). By measuring the volume within the nucleus that is occupied by heterochromatin, we find that heterochromatin constitutes ∼4% (±2%) of the nuclear volume.

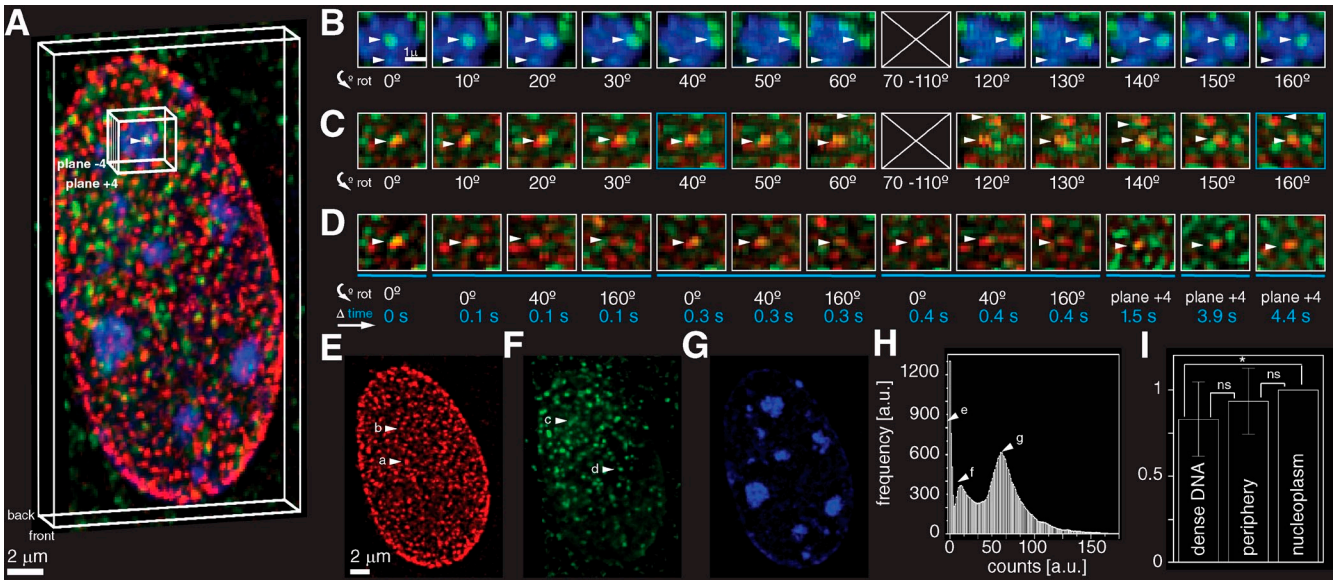

Figure 5. **3D distribution of β-actin mRNA within the nucleus of living cells.** (A) 3D projection of a nucleus showing β-actin mRNA carrying a 24× MS2 stem-loop cassette labeled with eYFP-MS2 coat protein (green), NPCs labeled with POM121-tdTomato (red), and heterochromatin DNA labeled with the vital dye Vybrant DyeCycle Violet (blue). The view is a time projection (β-actin mRNA, 5 s; NPC, 0.3 s; DNA, 1 s) rotated 10° around the y axis. The less intense clouds of signal represent mobile mRNA over this time span and spots represent immobile mRNAs (Video 2). The white box indicates the region of interest of the nucleus shown in B–D. (B) Zoomed in rotational view of β-actin mRNA (green) and heterochromatin (blue). Numbers below the images indicate the rotation angle. Arrowheads point at two mRNA clusters that appear to colocalize with heterochromatin. Whereas the upper cluster sits on top of the chromatin (40°–120°), the lower cluster is located within the heterochromatin. Projection was done without interpolation resulting in line patterns close to the 90° view (e.g., see 60°) and are therefore not displayed. The full 360° rotation is shown in Video 3. (C) Rotational view of β-actin mRNA and NPCs analogue to B. At all angles the β-actin mRNA partially overlaps with an NPC (bottom arrow). The full 360° rotation is shown in Video 4. B and C are static projections of the first frame of the videos. (D) Time course of β-actin mRNA and NPCs from three rotational perspectives. The 40° and 160° views for the 0-s time point are shown in C with blue frames. The mRNA–NPC interaction is most visible at an angle of 0° and invisible from the opposite side of the cell (160°) and ultimately nonproductive (mRNA arrives and leaves NPC on the same side). The last three views are from the first slices of the stack at an angle of 0° at later time points of the same video, illustrating repeated activity of a specific nuclear pore over time. Cyan bars under images indicate identical time groups. (E) Nuclear pore 3D projection from A. Arrowheads point to nuclear pores at the top/plane +4 (a) and bottom/plane −4 (b) of the nucleus. (F) 3D projection of the RNA channel from A. Arrowheads point to examples of a mobile β-actin mRNA resulting in a blurred projection (c) and a stationary β-actin mRNA resulting in a sharp projection (d). (G) 3D projection of the DNA channel from A. (H) Intensity frequency histogram of the cell (n = 1) in F showing three distributions: to the left, background resulting from rotation of the deconvolved image (arrowhead e); a lower intensity peak resulting from mobile mRNAs in the time projection (arrowhead f); and, to the right, a higher intensity peak resulting from stationary mRNAs in the time projection (arrowhead g). (I) Bar graph showing the level of β-actin mRNA localized to heterochromatin and heterochromatin periphery relative to nucleoplasm. On average a slight reduction of mRNA occupation in the heterochromatin was found, but was not statistically relevant (two-sided test). *, significant within 2σ confidence interval on the standard deviation; ns, not significant. Images were processed as described in Materials and methods and contrast was adjusted for visibility.

Distribution of β-actin mRNA in the nucleus

We were particularly interested in determining if β-actin mRNA is able to access heterochromatin regions and, if so, to what degree. We found that β-actin mRNA distributed almost uniformly across nucleoplasm, periphery, and heterochromatin (Fig. 5 I). We do not find a significant difference in β-actin mRNAs between the nucleoplasm and periphery, or between the periphery and heterochromatin volumes (Fig. 5 I). The definition of periphery attributes to the limited resolution of light microscopes and both nucleoplasm and periphery are defined without a positive marker. If we ignored the periphery and hence biased the two-sided nature of the appropriate statistical test, we found a significant 17% reduction of β-actin mRNA in heterochromatin compared with the nucleoplasm.

The only area within the nucleus with evident exclusion of β-actin mRNA is the nuclear envelope, other than at NPCs during export or scanning along the edge of the nuclear envelope. The number of export events recorded is small, likely caused by the longer integration time compared with the original study on β-actin mRNA export in these cells. We do observe that those pores that transported β-actin mRNA before are repeatedly active over time (Fig. 5 D). In summary, the distribution of β-actin mRNA in the nucleus is not uniform, but no areas are devoid of β-actin mRNA, including DNA-dense areas. Rather, we find that over a 5-s time interval β-actin mRNAs inhabit on average ∼5% ± 1% of the total nuclear volume. With the advantage of being able to simultaneously follow mRNA distribution and movement within the living cell along x, y, and z axes, in real time, this number accounts for 3D diffusion of β-actin mRNAs. The total number of voxels were counted that were occupied by RNA signals at a given time point, corresponding to a 100-ms time window that minimizes mobility effects on the distribution of the mRNAs. We found cell-to-cell variations in total voxel numbers ranging from a lower limit of ∼2,200 voxels to an upper limit of ∼7,200 voxels with a mean of ∼5,100 ± 1,400 voxels being occupied by β-actin mRNAs. At the achieved spatial sampling of 160 nm in x and y directions and 250 nm in z direction, a diffraction-limited spot will generate 12 voxels of signal. The variation in β-actin mRNA numbers is well explained by variation in expression levels from cell to

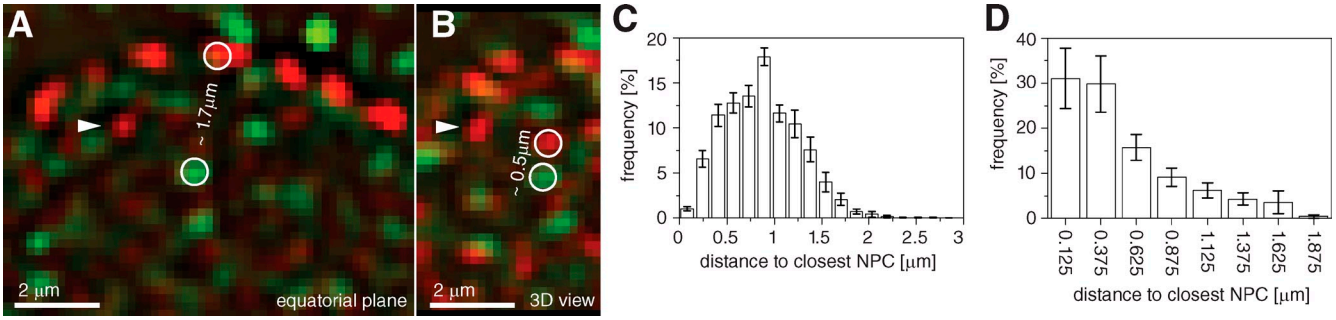

Figure 6. **Distance between mRNA and nuclear envelope.** (A) Region of interest view of the equatorial plane of Fig. 5 A. The closest distance between the circled mRNA and an NPC is close to 2 µm. The arrowhead points at a presumably closer NPC. (B) Rotated view of a 3D projection of the same mRNA. A NPC is found in close proximity to the mRNA two planes above. Arrowhead points to the same NPC as in A showing that the NPC is located one plane above the mRNA in A. (C) For all identified mRNA signals the closest lateral nuclear pore is identified and the distance measured. Most mRNAs (>80%) are further than 0.5 µm away from the nuclear rim. (D) For all identified mRNAs the shortest distance to a nuclear pore is calculated in 3D. At least 60% of mRNAs are within 0.5 µm of a nuclear pore and no more than 15% of mRNAs are further than 1 µm from a nuclear pore. The data are standard deviations per bin over 12 cells in which >51,000 distances between mRNAs and NPCs were measured.

cell. To exclude the possibility that the observed variation in β-actin mRNA occupancy could be caused by image processing, we performed two-way analysis of variance of the variation in total number of β-actin mRNA-occupied voxels between cells, which we found to be significant. When testing for variation in β-actin mRNA density rather than total number of β-actin mRNA-occupied voxels the analysis of variance yields no significant differences, indicating that the observed β-actin mRNA density is comparable between cells.

β-Actin mRNAs are always close to nuclear pores

In the equatorial plane the distance between mRNA and NPCs can be multiple micrometers and is limited by the size of the nucleus (Fig. 6 A). However, in cultured cell lines, the nucleus is often disk shaped, and the top and bottom are visible within our imaging volume. The radius of the nucleus in the z-direction is hence comparable to the height of our imaging volume (2.25 µm). Logically the height of the nucleus should dominate the actual distance between mRNA and the nuclear envelope. To understand this actual distance distribution between mRNA and the nuclear periphery, we identified the shortest lateral and axial distance between every mRNA and the closest nuclear pore using a nearest neighbor algorithm. Query of the lateral (x and y axis) distance between β-actin mRNA in any of our nine image planes to the closest NPC revealed that ∼95% of β-actin mRNA are observed within 1.5 µm from a NPC (Fig. 6, A and C). The 2D contour size of a nucleus in our mouse embryonic fibroblast cell line is roughly given by an oval with a shorter axis of ∼8 µm and a longer axis of ∼20 µm. In other words, if the analysis of nuclear space occupancy by mRNA was based on data acquired only in the equatorial plane of the cell, it could be incorrectly concluded that the center of the nucleus contains less β-actin mRNA than the nuclear periphery. If we instead analyze the 3D occupancy of nuclear volume by mRNA, querying the distance distribution for β-actin mRNA to the closest NPC in the z-direction we find >0% of β-actin mRNAs within 0.5 µm and >90% of β-actin mRNA within 1-µm distance of a nuclear pore (Fig. 6, B and D). The size correlation between the thickness of the nucleus and the imaging volume, both in the range of 2 µm, implies that a distance of 1 µm between mRNA and NPC is an upper limit along the z axis. Only ∼30% of β-actin mRNA were found within 0.5 µm of a nuclear pore in the lateral direction.

Discussion

Early studies of intranuclear mRNA movement presented the possibility that distinct tracks or pathways exist from the transcription site to the nuclear pore (Blobel, 1985; Edgar et al., 1986; Lawrence et al., 1989; Davis and Ish-Horowicz, 1991; Agutter, 1994). Later studies, however, have shown that this is not the case; that is, mRNA movement within the nucleus is diffusive and distributes throughout the intranuclear space (Zachar et al., 1993; Dirks et al., 1995; Femino et al., 1998; Daneholt, 1999; Politz et al., 1999; Singh et al., 1999). There are, however, findings that demonstrate this is not the entire picture. For example, gene activity was shown to correlate with chromatin territories (Stadler et al., 2004); a study based on the kinetic analysis of single human dystrophin mRNAs in U2OS cells suggests that mRNA mobility is facilitated in regions of low DNA density (Mor et al., 2010); the TREX complex was shown to couple to the NPC, thereby linking gene expression to nuclear transport (Cremer et al., 2006; Jani et al., 2012; Umlauf et al., 2013; Wickramasinghe et al., 2014); and upon depletion of ATP from the nucleus, the movement of β-actin mRNA is inhibited, indicating that mRNA mobility in the nuclear landscape requires energy (Shav-Tal et al., 2004).

In the last decade, kinetic studies using modern light microscopy in living cells painted a highly dynamic picture of the nucleus (Phair and Misteli, 2000; Shav-Tal et al., 2004; Grünwald et al., 2006b, 2008). Recombinant and endogenously fluorescent-tagged nuclear proteins and RNAs or fluorescent beads loaded into the nucleus were used to probe nuclear mobility and interactions with specific nuclear compartments like heterochromatin or the nucleolus (Görisch et al., 2004; Handwerger et al., 2005; Politz et al., 2006; Richter et al., 2007). In most of these biophysically oriented studies, different mobile

particles were recorded in one fluorescent channel simultaneously with fluorescently tagged nuclear compartments in a second fluorescent channel. From these studies, a divergent picture of nuclear organization arises: single molecules and particles of almost any size (up to ∼50 nm) can access any portion of the nuclear space, even including densely packed heterochromatin regions (Görisch et al., 2004; Grünwald et al., 2008). Large populations of molecules, such as polyA mRNAs, have been shown to move in the nucleus in the range of 1 $\mu m^2/s$ by use of fluorescence correlation spectroscopy (Politz et al., 2006). Interestingly, what was thought to be an exclusion of proteins from the nucleolus instead correlated with a lower retention rate and hence a higher mobility of proteins in the nucleolus compared with the nucleoplasm and heterochromatin regions (Grünwald et al., 2008). What these studies had in common was that the molecules in the nucleus were not constrained.

Our data represent the first full 3D analysis of the dynamic mobility, occupation, and interaction of a typical nuclear particle, β-actin mRNA, within the nuclear environment. We do not find evidence of exclusion from, or enrichment in, the heterochromatin, nor do we find repeated tracks of β-actin mRNAs occupying the same region of the nucleus on their travel to the nuclear envelope. Our data add that most β-actin mRNA (>60%) are <500 nm from the central channel of a NPC. At the same time β-actin mRNA appears to be traveling freely through the complex landscape of the nucleus.

These findings were possible by applying MFM to the simultaneous 3D imaging of mRNAs in the nucleus of a live cell. The acquisition of nine planes in a 3D signal allows the tracking of particles with a slower frame rate than in 2D, as particles are not lost as a result of being out of focus. However, faster frame rates than 100 ms per stack are needed to reduce blurring of the signal and to enable precise tracking of individual mRNAs over time. As a result we based our analysis on the measurement of voxels that mRNA occupied for each time point. A slower imaging rate means that more photons can be collected per time point, but a substantial amount of signal is lost as a result of lower efficiencies of the 3D components because MFG, chromatic correction grating (CCG), and prisms are theoretically ∼60% light efficient. The distribution of the signal in z-direction suffers from image distortion. We were able to measure these distortions in each cell and apply image registration and restoration to compensate. This was possible using a cell internal registration marker. We developed three major image analysis components: geometric descriptor matching to orient the image planes correctly, image entropy analysis to find the chromatically corrected z position for each plane, and analytical description of spherical aberration along the z axis necessary before image deconvolution.

We showed that 3D-SMRT microscopy is applicable to living cells at tolerable excitation power levels. Using a cell internal registration marker, similar to the super-registration concept for 2D alignment of nuclear pores (Grünwald and Singer, 2010), we developed a robust, feature-based image-alignment method that can be adjusted to the amount of registration features, supports different transformation models, and, in this case, was used to achieve global alignment of the MFM data with 0.5-pixel precision. With the alignment signal originating from within the sample, the degree of homogeneity in distribution of registration features across the image is known and possible optical aberrations introduced by the cell are corrected for. Although the current sampling rates, both in time and space, leave room for improvement, they are in the range of some 2D single-molecule imaging data (Semrau et al., 2011) and provide better time resolution than in comparable studies on nuclear organization (Mor et al., 2010). Although substantially faster 2D tracking data have been reported (Grünwald et al., 2006a; Grünwald and Singer, 2010; Manley et al., 2010), the ability to acquire 3D data translates into an extended focal depth (here about three times larger than in the 2D case) and a reduced chance of losing particles in the same time interval used in 2D imaging. Acquisition speed therefore can be slower, depending on the field of view and the total focal depth. The technology for faster imaging is already available with scientific complementary metal-oxide semiconductor cameras and larger, faster chips in electron multiplying charge coupled device (EMCCD) cameras. This means that signal currently limits the image acquisition speed. Improvements in signal strength are hence desirable and should ideally come from improved technology for labeling biomolecules and background reduction, as reduced excitation power is desirable in parallel to increased signal. The complex shape of the nuclear envelope and the distance between mRNA and nuclear pore in a living cell are two examples of why studies of molecular interactions in living cells need to account for anisotropy or nonlinearity of the cellular environment using simultaneous 3D-imaging approaches.

Materials and methods

Cell lines

In the mouse fibroblast cell line used, all β-actin mRNA carry a 24× MS2 stem loop cassette in the 3′ UTR that is labeled by eYFP fused to an MS2 protein tag. This cell line also harbors POM121 protein labeled with tdTomato fluorescent protein. POM121 exists in at least eight copies per NPC but tdTomato intensity only shows a three-modal labeling distribution (Grünwald and Singer, 2010; Lionnet et al., 2011). Cells were maintained in Iscove's modified Dulbecco's medium, supplemented with 10% FBS and penicillin/streptomycin. For microscopy, cells were cultured overnight on glass bottom dishes (MatTek Corporation) in Iscove's modified Dulbecco's medium + FBS. Before imaging, the media was changed to L15 (Gibco) supplemented with 10% FBS and cells were transferred to a CO_2-free incubator until use. To label DNA-rich compartments, Vybrant DyeCycle Violet (Life Technologies) was used. A total of 1 µl of dye at 5-mM concentration was added directly to the L15 media (2 ml) and cells were incubated at 37°C for 30 min before imaging. Cells were imaged at room temperature using Solis for acquisition (Andor Technology).

Imaging system

We used a multifocus microscope (Fig. 1; Abrahamsson et al., 2013). To achieve separation of the light collected by the objective into multiple planes, a secondary pupil plane (Fourier plane) was formed inside a relay optic (L1 and L2) in which a distorted diffractive MFG was placed, similar to Blanchard and Greenaway (1999). The MFG was followed by a CCG and a refractive prism (Fig. 1). In the primary image plane behind the microscope's tube lens, a square iris was placed to restrict the size of the image or field of view. The MFG splits the fluorescence light emitted from the sample into its zero and first diffractive orders, resulting in nine beams of similar intensity (Mait, 1995). The pattern of the MFG is distorted, introducing an angular offset to each image corresponding to a 2D diffractive order (m_x and m_y) of the grating. The CCG corrects for chromatic dispersion and was placed behind the MFG at a position where the diffractive orders were separated. A multifaceted refractive prism was used to redirect

the individual beams toward the second lens of the relay optic that forms nine images on the camera. Color separation and band-pass filtering was done using a custom-made optic (dichroic mirror: 6-mm thickness, 2-in diameter with λ/10 flatness; band-pass for eYFP and tdTomato; Chroma Technology Corp.).

The design of MFG, CCG, and prism assumed a refractive index (RI) of 1.4 and a NA of 1.3. These values are closely matched using a 60× silicone immersion objective with an NA of 1.3 and RI of 1.41 for the immersion media. The effective maximal detection NA is given by multiplying the NA of the objective with the RI of the sample/buffer divided by the RI of the objective immersion. The expected effective or detection NA of the microscope is hence 1.3 × 1.41/1.33 = 1.23. Using beads for calibration, we estimated the effective detection NA at 1.2, well in agreement with our expectation. The deviation from the design value for the NA, the effective NA being 1.2 rather than the expected 1.3, results from imaging live cells in aqueous solution with a RI different from that of the objective immersion.

The need for a large field of view, high sensitivity, and high time resolution (100 ms per frame) was met using 780 × 761-pixel subregions on two back-illuminated EMCCDs (model 888, built in 2011; Andor Technology). The pixels of this camera have a side length of 13 µm. The relay optic with L1 being a 150-mm lens and L2 being a 200-mm lens introduces a slight magnification of 1.3×. Together, the total magnification of objective (60×) and MFM (1.3×) was 80×, resulting in a pixel size in image space of 162.5 nm in x and y. The z-spacing is given by the MFG design and is 250 nm for the used grating. The size of the PSF can be estimated and $\sigma_{\text{PSF-full width}}$ at 534 nm equals ∼270 nm in x and y and ∼520 nm in z. The full width at half maximum of the detected signal is defined as 2.355 × σ and is accordingly ∼320 nm in x and y and ∼610 nm in z. For the mRNA labeled with eYFP, these values result in lateral undersampling of the PSF and axial Nyquist sampling. Color separation on the two cameras was done with an ultra flat dichroic mirror positioned after L2.

For fluorescence excitation, three lasers, 405 (Cube; Coherent), 514 (Sapphire; Coherent), and 561 nm (Melles Griot), were combined into a single optical fiber and delivered to the microscope. Image acquisition was done with two identical cameras where mRNA (eYFP, 514-nm laser) and nuclear pores (tdTomato, 561-nm laser) were acquired simultaneously, whereas registration data were recorded immediately after (Vybrant DyeCycle Violet, 405-nm laser). The maximal cumulative excitation power was ∼600 µW. For registration, two datasets were taken. First a 10-frame-long (= 1 s) 3D time series was recorded of the nucleus with the same parameters used for mRNA and nuclear pore imaging. Next a fine registration dataset was recorded where the 3D acquisition beam was z-stacked through the nucleus in 10-nm steps using an objective stage (Piezo).

Image registration marker

Use of cell external registration markers was impossible because of the need to fit nine planes on one camera chip while maximizing the acquisition speed. The resulting field of view allows capturing the whole nucleus but not much of the cytoplasm or even the extracellular space. To achieve the highest degree of physical alignment and confidence, a cell internal marker is favorable. Such a marker would need to emit over the whole spectrum used in the experiment and would have to be switchable between on and off states so as to not overlay the fluorescent signal of the sample. A DNA marker, Vybrant DyeCycle Violet, fits this bill. Binding to double-stranded DNA the dye emits a strong signal spanning from 400 to 700 nm when excited at ∼400 nm. The strong fluorescence emission of the dye allows for excitation with minimal amounts of light.

Photodamage through low-level laser light excitation has been described previously (Carlton et al., 2010). In a straightforward experiment, the doubling rate of yeast cells on the microscope was measured and a reduction was found with <100 µW of input power at the back-focal plane. At 0.8 mW of input power cell growth was practically arrested. The experiment was done using 488- and 561-nm laser light, demonstrating higher sensitivity to blue than red light. Shifting the wavelength down to 405 nm hence is likely to impact cells even at very low power levels.

To avoid the possibility that our mRNA data are impacted by the registration procedure, the registration images were recorded immediately after acquiring the mRNA and NPC data. Similarly, the possibility of damage to neighboring cells by general imaging conditions cannot be excluded or monitored in our experiments (Dobrucki et al., 2007). We hence imaged only a few well-separated cells per dish. Under these imaging conditions, the Vybrant DyeCycle Violet provided an acceptable independent alignment marker based on the distribution of DNA in the nucleus, yielding additional information about nuclear occupation by DNA. The fact that the registration is taken independently from data acquisition is unavoidable and adds a possible source of error to the assumed static distribution of DNA during the duration of imaging.

Image registration in silico

The software is implemented in ImgLib2 (Pietzsch et al., 2012) and available on GitHub (https://github.com/StephanPreibisch/MFM-Align), published under the GPLv3 license. The redundant geometric local descriptor matching is available on GitHub (https://github.com/bigdataviewer/Descriptor_based_registration) and as a Fiji plugin distributed through the Fiji Updater (Schindelin et al., 2012; http://fiji.sc/Downloads. It can be found under Plugins > registration > Descriptor based Registration (2d/3d) and Plugins > registration > Descriptor based Series Registration (2d/3d+t).

Image registration precision

Image plane registration is achieved through detection of corresponding image features and fitting of a transformation model that minimizes the distances between all corresponding features. The number and distribution of corresponding features within the image, localization precision, and the transformation model influence the final quality of the registration.

To achieve optimal registration quality, the transformation model should require a minimal amount of parameters to solve, while still being able to describe all significant transformations that occur during acquisition. As the remaining distance between corresponding features after applying the transformation is normally distributed (Fig. 4, A and B), maximizing the number of corresponding features will minimize the final registration error and at the same time provide a high confidence that the registration result is correct. In other words, being able to identify thousands of corresponding detections that all support the same transformation model (requiring two corresponding features to be solved) shows that the conservative approach of using a rigid transformation model is sufficient to achieve registration precision of 0.5 pixels (Fig. 4). Feature-based image registration currently supports regularized translation, rigid, similarity, affine, and homography transformation models and is available both as source code (in online supplemental material) or Fiji function.

To test and compare feature-based registration against alignment with diffraction-limited beads, we labeled 1-µm beads (nonfluorescent NeutrAvidin labeled FluoSpheres; Life Technologies) with biotinylated plasmid DNA (*Label* IT; Mirus) and stained with Vybrant DyeCycle Violet. The beads were embedded in an agarose gel and imaged in the green and red MFM channel. Registration was done for the beads as for the cells. As a control we embedded 0.2-µm-diameter TetraSpeck beads (Life Technologies) in the same gel. This allows direct comparison of a Gaussian fit–based alignment of diffraction-limited spots to our quadratic fit using feature-based alignment (Fig. 4 C).

Image deconvolution

As originally reported, MFM using a single MFG for a wide range of emission light bandwidth (here eYFP and tdTomato) will produce a wavelength-dependent defocus. In real-live applications the experimental conditions might not always match the optical design to the number, adding an additional source of image distortion. As discussed in the Imaging system section, the use of living cells in an aqueous buffer resulted in a mismatch of the refractive index between objective immersion and sample. This situation is common to the use of high NA objectives, but because of the inherent 3D nature of our image acquisition the spherical aberrations introduced on top of the expected defocus need to be taken into account in image processing.

A defocus is necessary to focus at a distance Δz in the sample depending on the optical path difference between the ray over the optical axis and under an angle θ (Abrahamsson et al., 2013), as described in the following equation:

$$D_i = \Delta z\left(k_i - k_{z_i}\right) = n_i \Delta z k_0 \left(1 - \sqrt{1 - \frac{k_x^2 + k_y^2}{k_i^2}}\right) = n_i \Delta z k_0 \left(1 - \cos\theta_i\right).$$

Here n_i is the refractive index of media i, k_0 is the length of the wave vector in vacuum, k_{z_i} is the wave vector length of the z component in media i, and Δz is the thickness of the medium. The differences in sign and constant phase offset to the original publication can be ignored. In addition to the original approach, we had to compensate for the spherical aberration introduced by refractive index mismatch. The spherical aberration (SA)

caused by index of refraction mismatch (Braat, 1997; Stallinga, 2005) is given by:

$$SA_{1,2} = \Delta z\left(k_1 - k_{z_1}\right) - \Delta z\left(k_2 - k_{z_2}\right) = n_1 \Delta z k_0 \left(1 - \cos\theta_1\right) - n_2 \Delta z k_0 \left(1 - \cos\theta_2\right).$$

Here, Δz is the thickness of medium 2, θ_1 is the angle in medium 1, and θ_2 is the angle in medium 2. Note that this expression does not only contain spherical aberration (of all orders) but also defocus. After estimation and correction of the z-dependence of spherical aberrations in each dataset (Fig. 3), a momentum-preserving deconvolution with the distorted PSF is done to completely correct for limits of the used MFG, using Huygens professional software (SVI). Momentum-preserving deconvolution was done on the aligned image volumes without further image processing. For display, image contrast was adjusted and the resolution (dpi) was adjusted without interpolation. All analysis was preformed on the deconvolved, registered images. A 3D smoothing (σ1 pixel) was applied to the DNA channel.

mRNA detection

Signal variability causes difficulty in separating noise from real fluorescence. This is because of unbound fluorescently labeled MS2 coat proteins, out of focus mRNA particles located in other planes along the optical axis, autofluorescence of the cell, as well as the limited spectral separation of eYFP and tdTomato (Grünwald and Singer, 2010). A simple threshold for particle identification is highly error prone, which led us to using the methodology of scale space where we can search for Gaussian structures that have the width of a diffraction-limited spot while simultaneously estimating and subtracting the local background variations. To create comparability between different cells, a uniform parameter is needed to be able to discriminate between spots originating from noise and signal. This was done by sorting the intensities of all candidate mRNAs for intensity and selecting the stationary point of the obtained graph as the discriminatory threshold of noise versus signal (β-actin mRNA). The DNA channel was smoothed with a Gaussian filter (σ = 1) and then binary thresholds were used to segment the nucleus.

Online supplemental material

Four videos relating to Figs. 2 and 5 can be found as supplemental material. Video 1 shows the before and after lateral alignment of the MFM image stacks using feature-based registration. Video 2 shows the first 50 frames of the time series of the cell shown in Fig. 5 A. Video 3 shows the DNA and mRNA signal from a subregion of this cell with 1° rendering of the 3D rotation shown in Fig. 5 B. Video 4 shows the NPC and mRNA signal from a subregion of this cell with 1° rendering of the 3D rotation shown in Fig. 5 C. The source code for 3D alignment of MFM volumes using feature-based alignment is available here and on GitHub (https://github.com/StephanPreibisch/MFM-Align). We suggest cloning the project from GitHub, where any questions, remarks, or issues regarding the software can be posted. The mpicbg package is hosted on GitHub (https://github.com/axtimwalde/mpicbg) as is the descriptor-based registration package (https://github.com/bigdataviewer/Descriptor_based_registration). Maven manages all other dependencies, including those two. Simply importing this project as "Existing Maven Project" into Eclipse (https://www.eclipse.org/downloads) will make the executable as well as source code available. The zip file of the current version in the online supplemental material contains a README.md file with general comments on the project, a pom.xml file that holds the definitions of the Maven project, and a source directory (src) containing all source code files. Online supplemental material is available at http://www.jcb.org/cgi/content/full/jcb.201411032/DC1.

We dedicate this paper to the memory of the late Mats G.L. Gustafsson, a pioneer in superresolution and 3D microscopy and the mentor with whom S. Abrahamsson developed the MFM technique.

The authors thank Helen White at Howard Hughes Medical Institute (HHMI) Janelia Farm for tissue culture support and Darryl Conte at RNA Therapeutics Institute, University of Massachusetts Medical School, for critical reading of the manuscript.

This work was supported by National Institutes of Health grants GM 57071 and NS 85083 EB 13571 and HHMI to R.H. Singer, S. Abrahamsson was supported by HHMI Janelia Farm in the laboratory of M.G.L. Gustafsson, S. Preibisch was supported by Howard Hughes Medical Institute (HHMI) in E. Myers' laboratory and the Human Frontier Science Program (HFSP) Postdoctoral Fellowship LT000783/2012 in R.H. Singer's and E. Myers' laboratory.

The authors declare no competing financial interests.

Submitted: 10 November 2014
Accepted: 21 April 2015

References

Abrahamsson, S., J. Chen, B. Hajj, S. Stallinga, A.Y. Katsov, J. Wisniewski, G. Mizuguchi, P. Soule, F. Mueller, C. Dugast Darzacq, et al. 2013. Fast multicolor 3D imaging using aberration-corrected multifocus microscopy. *Nat. Methods*. 10:60–63. http://dx.doi.org/10.1038/nmeth.2277

Agutter, P.S. 1994. Models for solid-state transport: messenger RNA movement from nucleus to cytoplasm. *Cell Biol. Int.* 18:849–858. http://dx.doi.org/10.1006/cbir.1994.1121

Backlund, M.P., M.D. Lew, A.S. Backer, S.J. Sahl, G. Grover, A. Agrawal, R. Piestun, and W.E. Moerner. 2012. Simultaneous, accurate measurement of the 3D position and orientation of single molecules. *Proc. Natl. Acad. Sci. USA*. 109:19087–19092. http://dx.doi.org/10.1073/pnas.1216687109

Blanchard, P.M., and A.H. Greenaway. 1999. Simultaneous multiplane imaging with a distorted diffraction grating. *Appl. Opt.* 38:6692–6699. http://dx.doi.org/10.1364/AO.38.006692

Blobel, G. 1985. Gene gating: a hypothesis. *Proc. Natl. Acad. Sci. USA*. 82:8527–8529. http://dx.doi.org/10.1073/pnas.82.24.8527

Braat, J. 1997. Influence of substrate thickness on optical disk readout. *Appl. Opt.* 36:8056–8062. http://dx.doi.org/10.1364/AO.36.008056

Brown, M., and D.H. Lowe. 2002. Invariant features from interest point groups. *In* International Conference on Computer Vision, Cardiff, Wales. 656–665.

Carlton, P.M., J. Boulanger, C. Kervrann, J.B. Sibarita, J. Salamero, S. Gordon-Messer, D. Bressan, J.E. Haber, S. Haase, L. Shao, et al. 2010. Fast live simultaneous multiwavelength four-dimensional optical microscopy. *Proc. Natl. Acad. Sci. USA*. 107:16016–16022. http://dx.doi.org/10.1073/pnas.1004037107

Cook, P.R., and D. Marenduzzo. 2009. Entropic organization of interphase chromosomes. *J. Cell Biol.* 186:825–834. http://dx.doi.org/10.1083/jcb.200903083

Cremer, T., M. Cremer, S. Dietzel, S. Müller, I. Solovei, and S. Fakan. 2006. Chromosome territories—a functional nuclear landscape. *Curr. Opin. Cell Biol.* 18:307–316. http://dx.doi.org/10.1016/j.ceb.2006.04.007

Daneholt, B. 1999. Pre-mRNP particles: From gene to nuclear pore. *Curr. Biol.* 9:R412–R415. http://dx.doi.org/10.1016/S0960-9822(99)80256-5

Davis, I., and D. Ish-Horowicz. 1991. Apical localization of pair-rule transcripts requires 3′ sequences and limits protein diffusion in the *Drosophila* blastoderm embryo. *Cell*. 67:927–940. http://dx.doi.org/10.1016/0092-8674(91)90366-7

Dirks, R.W., K.C. Daniël, and A.K. Raap. 1995. RNAs radiate from gene to cytoplasm as revealed by fluorescence in situ hybridization. *J. Cell Sci.* 108:2565–2572.

Dobrucki, J.W., D. Feret, and A. Noatynska. 2007. Scattering of exciting light by live cells in fluorescence confocal imaging: phototoxic effects and relevance for FRAP studies. *Biophys. J.* 93:1778–1786. http://dx.doi.org/10.1529/biophysj.106.096636

Edgar, B.A., M.P. Weir, G. Schubiger, and T. Kornberg. 1986. Repression and turnover pattern *fushi tarazu* RNA in the early *Drosophila* embryo. *Cell*. 47:747–754. http://dx.doi.org/10.1016/0092-8674(86)90517-9

Femino, A.M., F.S. Fay, K. Fogarty, and R.H. Singer. 1998. Visualization of single RNA transcripts in situ. *Science*. 280:585–590. http://dx.doi.org/10.1126/science.280.5363.585

Fischler, M.A., and R.C. Bolles. 1981. Random sample consensus: a paradigm for model fitting with applications to image analysis and automated cartography. *Commun. ACM*. 24:381–395. http://dx.doi.org/10.1145/358669.358692

Gibcus, J.H., and J. Dekker. 2013. The hierarchy of the 3D genome. *Mol. Cell*. 49:773–782. http://dx.doi.org/10.1016/j.molcel.2013.02.011

Görisch, S.M., M. Wachsmuth, C. Ittrich, C.P. Bacher, K. Rippe, and P. Lichter. 2004. Nuclear body movement is determined by chromatin accessibility and dynamics. *Proc. Natl. Acad. Sci. USA*. 101:13221–13226. http://dx.doi.org/10.1073/pnas.0402958101

Grünwald, D., and R.H. Singer. 2010. *In vivo* imaging of labelled endogenous β-actin mRNA during nucleocytoplasmic transport. *Nature*. 467:604–607. http://dx.doi.org/10.1038/nature09438

Grünwald, D., A. Hoekstra, T. Dange, V. Buschmann, and U. Kubitscheck. 2006a. Direct observation of single protein molecules in aqueous solution. *ChemPhysChem*. 7:812–815. http://dx.doi.org/10.1002/cphc.200500632

Grünwald, D., B. Spottke, V. Buschmann, and U. Kubitscheck. 2006b. Intranuclear binding kinetics and mobility of single native U1 snRNP particles in living cells. *Mol. Biol. Cell*. 17:5017–5027. http://dx.doi.org/10.1091/mbc.E06-06-0559

Grünwald, D., R.M. Martin, V. Buschmann, D.P. Bazett-Jones, H. Leonhardt, U. Kubitscheck, and M.C. Cardoso. 2008. Probing intranuclear environments at the single-molecule level. *Biophys. J.* 94:2847–2858. http://dx.doi.org/10.1529/biophysj.107.115014

Handwerger, K.E., J.A. Cordero, and J.G. Gall. 2005. Cajal bodies, nucleoli, and speckles in the *Xenopus* oocyte nucleus have a low-density, sponge-like structure. *Mol. Biol. Cell*. 16:202–211. http://dx.doi.org/10.1091/mbc.E04-08-0742

Huang, B., W. Wang, M. Bates, and X. Zhuang. 2008. Three-dimensional super-resolution imaging by stochastic optical reconstruction microscopy. *Science*. 319:810–813. http://dx.doi.org/10.1126/science.1153529

Jani, D., S. Lutz, E. Hurt, R.A. Laskey, M. Stewart, and V.O. Wickramasinghe. 2012. Functional and structural characterization of the mammalian TREX-2 complex that links transcription with nuclear messenger RNA export. *Nucleic Acids Res.* 40:4562–4573. http://dx.doi.org/10.1093/nar/gks059

Kubitscheck, U., T. Kues, and R. Peters. 1999. Visualization of nuclear pore complex and its distribution by confocal laser scanning microscopy. *Methods Enzymol.* 307:207–230. http://dx.doi.org/10.1016/S0076-6879(99)07015-9

Lawrence, J.B., R.H. Singer, and L.M. Marselle. 1989. Highly localized tracks of specific transcripts within interphase nuclei visualized by in situ hybridization. *Cell*. 57:493–502. http://dx.doi.org/10.1016/0092-8674(89)90924-0

Lionnet, T., K. Czaplinski, X. Darzacq, Y. Shav-Tal, A.L. Wells, J.A. Chao, H.Y. Park, V. de Turris, M. Lopez-Jones, and R.H. Singer. 2011. A transgenic mouse for in vivo detection of endogenous labeled mRNA. *Nat. Methods*. 8:165–170. http://dx.doi.org/10.1038/nmeth.1551

Mait, J.N. 1995. Understanding diffractive optic design in the scalar domain. *J. Opt. Soc. Am. A Opt. Image Sci. Vis.* 12:2145–2158. http://dx.doi.org/10.1364/JOSAA.12.002145

Manley, S., J.M. Gillette, and J. Lippincott-Schwartz. 2010. Single-particle tracking photoactivated localization microscopy for mapping single-molecule dynamics. *Methods Enzymol.* 475:109–120. http://dx.doi.org/10.1016/S0076-6879(10)75005-9

Misteli, T., A. Gunjan, R. Hock, M. Bustin, and D.T. Brown. 2000. Dynamic binding of histone H1 to chromatin in living cells. *Nature*. 408:877–881. http://dx.doi.org/10.1038/35048610

Mor, A., S. Suliman, R. Ben-Yishay, S. Yunger, Y. Brody, and Y. Shav-Tal. 2010. Dynamics of single mRNP nucleocytoplasmic transport and export through the nuclear pore in living cells. *Nat. Cell Biol.* 12:543–552. http://dx.doi.org/10.1038/ncb2056

Padeken, J., and P. Heun. 2014. Nucleolus and nuclear periphery: velcro for heterochromatin. *Curr. Opin. Cell Biol.* 28:54–60. http://dx.doi.org/10.1016/j.ceb.2014.03.001

Phair, R.D., and T. Misteli. 2000. High mobility of proteins in the mammalian cell nucleus. *Nature*. 404:604–609. http://dx.doi.org/10.1038/35007077

Pietzsch, T., S. Preibisch, P. Tomancák, and S. Saalfeld. 2012. ImgLib2—generic image processing in Java. *Bioinformatics*. 28:3009–3011. http://dx.doi.org/10.1093/bioinformatics/bts543

Politz, J.C., R.A. Tuft, T. Pederson, and R.H. Singer. 1999. Movement of nuclear poly(A) RNA throughout the interchromatin space in living cells. *Curr. Biol.* 9:285–291. http://dx.doi.org/10.1016/S0960-9822(99)80136-5

Politz, J.C., R.A. Tuft, K.V. Prasanth, N. Baudendistel, K.E. Fogarty, L.M. Lifshitz, J. Langowski, D.L. Spector, and T. Pederson. 2006. Rapid, diffusional shuttling of poly(A) RNA between nuclear speckles and the nucleoplasm. *Mol. Biol. Cell*. 17:1239–1249. http://dx.doi.org/10.1091/mbc.E05-10-0952

Preibisch, S., S. Saalfeld, J. Schindelin, and P. Tomancak. 2010. Software for bead-based registration of selective plane illumination microscopy data. *Nat. Methods*. 7:418–419. http://dx.doi.org/10.1038/nmeth0610-418

Ragan, T., H. Huang, P. So, and E. Gratton. 2006. 3D particle tracking on a two-photon microscope. *J. Fluoresc.* 16:325–336. http://dx.doi.org/10.1007/s10895-005-0040-1

Ram, S., P. Prabhat, J. Chao, E.S. Ward, and R.J. Ober. 2008. High accuracy 3D quantum dot tracking with multifocal plane microscopy for the study of fast intracellular dynamics in live cells. *Biophys. J.* 95:6025–6043. http://dx.doi.org/10.1529/biophysj.108.140392

Richter, K., M. Nessling, and P. Lichter. 2007. Experimental evidence for the influence of molecular crowding on nuclear architecture. *J. Cell Sci.* 120:1673–1680. http://dx.doi.org/10.1242/jcs.03440

Saalfeld, S., A. Cardona, V. Hartenstein, and P. Tomančák. 2010. As-rigid-as-possible mosaicking and serial section registration of large ssTEM datasets. *Bioinformatics*. 26:i57–i63. http://dx.doi.org/10.1093/bioinformatics/btq219

Schermelleh, L., P.M. Carlton, S. Haase, L. Shao, L. Winoto, P. Kner, B. Burke, M.C. Cardoso, D.A. Agard, M.G. Gustafsson, et al. 2008. Subdiffraction multicolor imaging of the nuclear periphery with 3D structured illumination microscopy. *Science*. 320:1332–1336. http://dx.doi.org/10.1126/science.1156947

Schindelin, J., I. Arganda-Carreras, E. Frise, V. Kaynig, M. Longair, T. Pietzsch, S. Preibisch, C. Rueden, S. Saalfeld, B. Schmid, et al. 2012. Fiji: an open-source platform for biological-image analysis. *Nat. Methods*. 9:676–682. http://dx.doi.org/10.1038/nmeth.2019

Semrau, S., L. Holtzer, M. González-Gaitán, and T. Schmidt. 2011. Quantification of biological interactions with particle image cross-correlation spectroscopy (PICCS). *Biophys. J.* 100:1810–1818. http://dx.doi.org/10.1016/j.bpj.2010.12.3746

Shav-Tal, Y., X. Darzacq, S.M. Shenoy, D. Fusco, S.M. Janicki, D.L. Spector, and R.H. Singer. 2004. Dynamics of single mRNPs in nuclei of living cells. *Science*. 304:1797–1800. http://dx.doi.org/10.1126/science.1099754

Shevtsov, S.P., and M. Dundr. 2011. Nucleation of nuclear bodies by RNA. *Nat. Cell Biol.* 13:167–173. http://dx.doi.org/10.1038/ncb2157

Singh, O.P., B. Björkroth, S. Masich, L. Wieslander, and B. Daneholt. 1999. The intranuclear movement of Balbiani ring premessenger ribonucleoprotein particles. *Exp. Cell Res.* 251:135–146. http://dx.doi.org/10.1006/excr.1999.4490

Sleeman, J.E., and L. Trinkle-Mulcahy. 2014. Nuclear bodies: new insights into assembly/dynamics and disease relevance. *Curr. Opin. Cell Biol.* 28:76–83. http://dx.doi.org/10.1016/j.ceb.2014.03.004

Stadler, S., V. Schnapp, R. Mayer, S. Stein, C. Cremer, C. Bonifer, T. Cremer, and S. Dietzel. 2004. The architecture of chicken chromosome territories changes during differentiation. *BMC Cell Biol.* 5:44. http://dx.doi.org/10.1186/1471-2121-5-44

Stallinga, S. 2005. Compact description of substrate-related aberrations in high numerical-aperture optical disk readout. *Appl. Opt.* 44:849–858. http://dx.doi.org/10.1364/AO.44.000849

Trinkle-Mulcahy, L., and A.I. Lamond. 2007. Toward a high-resolution view of nuclear dynamics. *Science*. 318:1402–1407. http://dx.doi.org/10.1126/science.1142033

Umlauf, D., J. Bonnet, F. Waharte, M. Fournier, M. Stierle, B. Fischer, L. Brino, D. Devys, and L. Tora. 2013. The human TREX-2 complex is stably associated with the nuclear pore basket. *J. Cell Sci.* 126:2656–2667. http://dx.doi.org/10.1242/jcs.118000

Wickramasinghe, V.O., R. Andrews, P. Ellis, C. Langford, J.B. Gurdon, M. Stewart, A.R. Venkitaraman, and R.A. Laskey. 2014. Selective nuclear export of specific classes of mRNA from mammalian nuclei is promoted by GANP. *Nucleic Acids Res.* 42:5059–5071. http://dx.doi.org/10.1093/nar/gku095

Zachar, Z., J. Kramer, I.P. Mims, and P.M. Bingham. 1993. Evidence for channeled diffusion of pre-mRNAs during nuclear RNA transport in metazoans. *J. Cell Biol.* 121:729–742. http://dx.doi.org/10.1083/jcb.121.4.729